Microstructures

Open Access

Check for updates

Supplementary Material: Tunable negative thermal expansion in La(Fe, Si)$_{13}$/resin composites with high mechanical property and long-term cycle stability

MAIN TEXT

Supplementary Figure 1 shows the temperature dependence of linear thermal expansions ($\Delta L/L$) for the epoxy resin. It can be found that the epoxy resin shows a positive thermal expansion behavior in a wide temperature range.

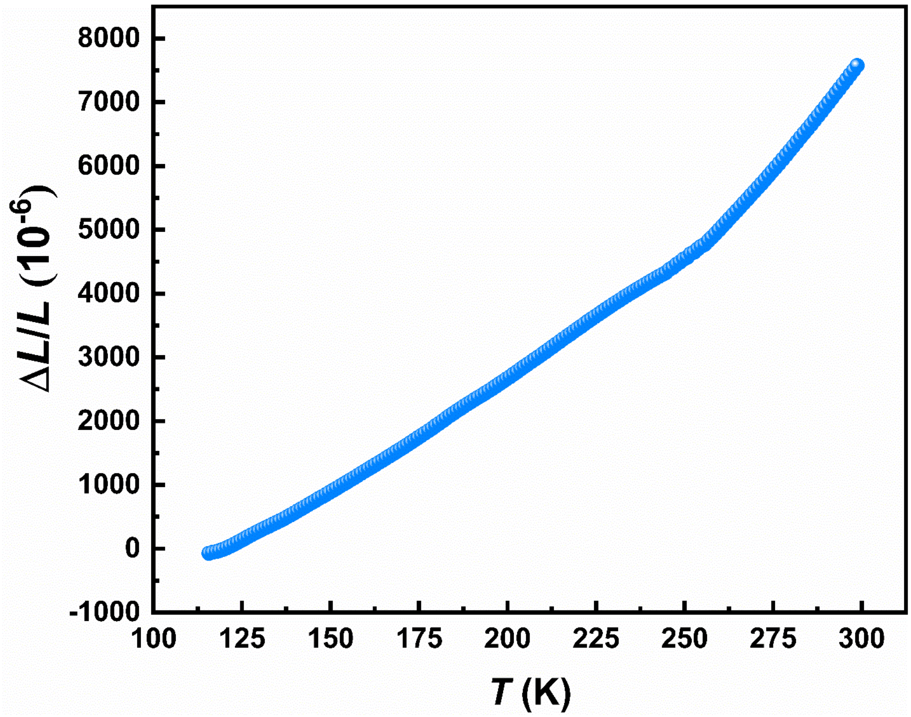

Supplementary Figure 1. Temperature dependence of linear thermal expansion ($\Delta L/L$) for the epoxy resin.

Supplementary Figure 2A shows the schematic illustration of the $La_{0.7}Ce_{0.3}Fe_{11.51}Mn_{0.09}Si_{1.4}$ powder preparation. The backscattered electron (BSE) image from SEM of the $La_{0.7}Ce_{0.3}Fe_{11.51}Mn_{0.09}Si_{1.4}$ ribbon is displayed in Supplementary Figure 2B. The phase composition of the ribbon is mainly the 1:13 phase, accompanied by a very small amount of α-Fe phase and La-rich phase.

Supplementary Figure 2C shows the Rietveld refined XRD pattern of the $La_{0.7}Ce_{0.3}Fe_{11.51}Mn_{0.09}Si_{1.4}$ powders at room temperature. It further confirms that the $La_{0.7}Ce_{0.3}Fe_{11.51}Mn_{0.09}Si_{1.4}$ compound mainly crystallizes into 1:13 phase with a small amount of α-Fe phase, i.e., the content of 1:13 phase and α-Fe phase obtained from refinement are 97.1 wt.% and 2.9 wt.%, respectively. The amount of La-rich phase is too low to be detected by the laboratory XRD measurement.

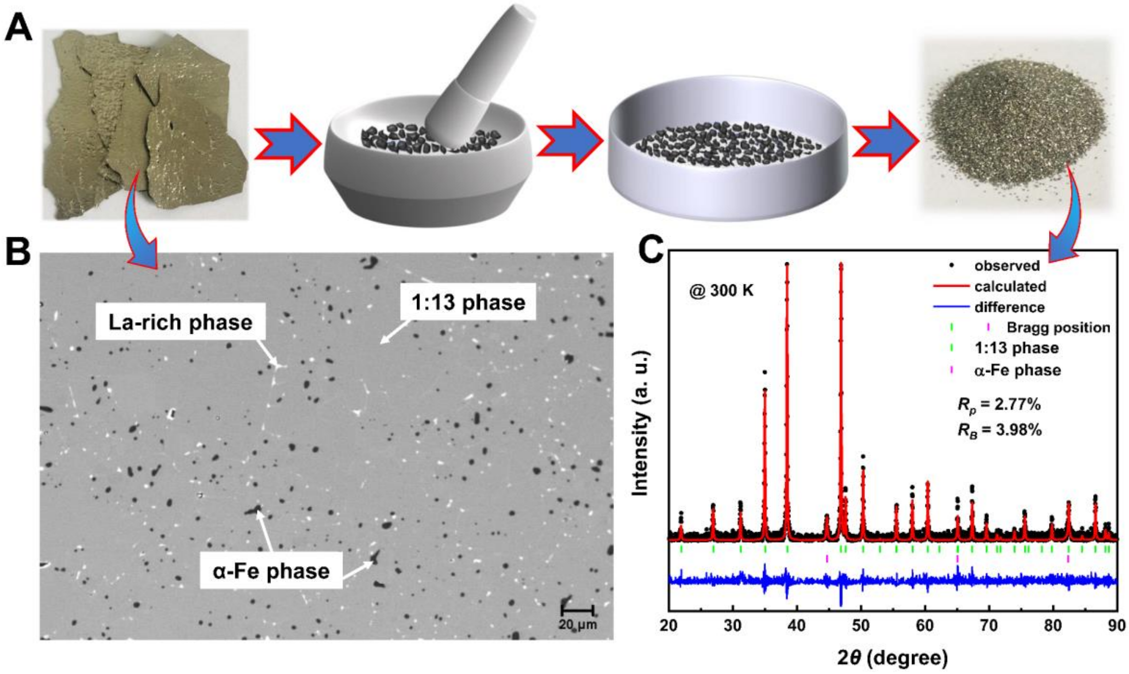

Supplementary Figure 2. (A) Schematic illustration of La-Fe-Si powders preparation; (B) Backscattered electron image of La-Fe-Si ribbon; (C) Observed and refined powder XRD patterns of La-Fe-Si powders.

Supplementary Figure 3 shows the size distribution of different groups of the $La_{0.7}Ce_{0.3}Fe_{11.51}Mn_{0.09}Si_{1.4}$ powders. The size distribution of these particles can be obtained from the SEM micrographs of these $La_{0.7}Ce_{0.3}Fe_{11.51}Mn_{0.09}Si_{1.4}$ powders. Gaussian fittings (green lines) demonstrate that the size distribution of these powders presents a unimodal normal distribution. Based on the Gaussian function analysis, the average particle diameters (d) and the standard deviation of these particles can be obtained. As shown in Supplementary Figure 3, they are 397.9 μm, 278.0 μm, 180.4 μm, 96.6 μm, 45.2 μm and 3.6 μm, respectively (hereafter refers to P398, P278, P180, P97, P45 and P4).

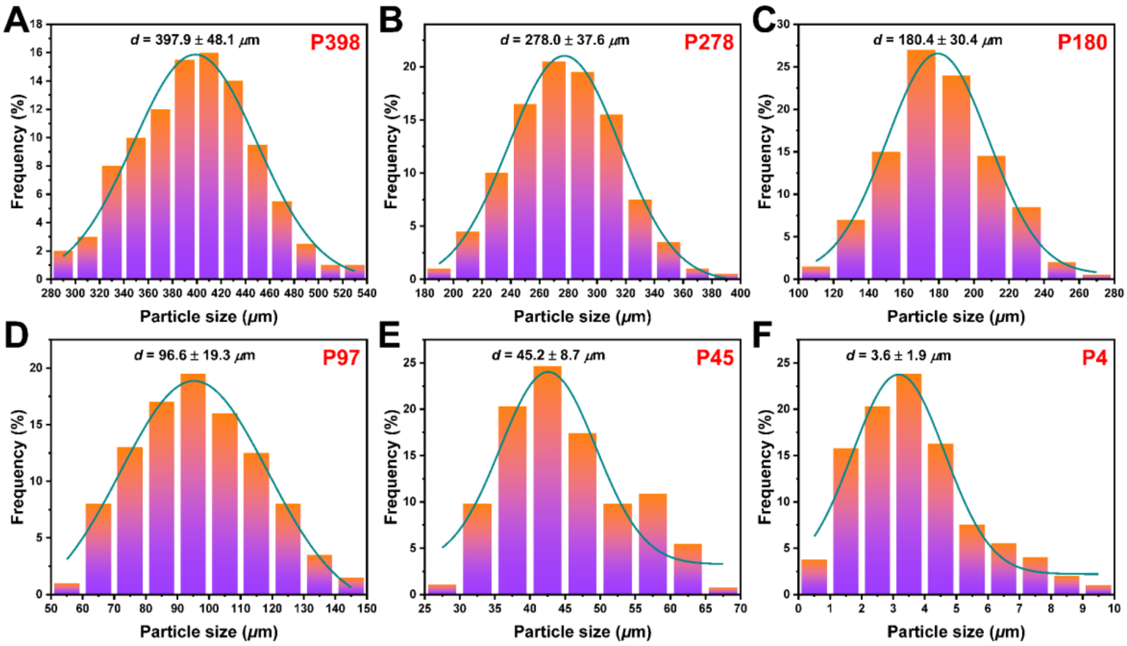

Supplementary Figure 3. Size distribution of different groups of the $La_{0.7}Ce_{0.3}Fe_{11.51}Mn_{0.09}Si_{1.4}$ powders.

Supplementary Figure 4A shows the temperature dependence of magnetization for the $La_{0.7}Ce_{0.3}Fe_{11.51}Mn_{0.09}Si_{1.4}$ compound with different particle sizes. The compound experiences a magnetic transition from PM to FM states, and the distinct thermal hysteresis indicates the typical characteristic of first-order magnetic transition. The T_C remains nearly constant with reduction of the particle sizes. However, the thermal hysteresis varies with decrease of the particle sizes. Supplementary Figure 4B displays the thermal hysteresis as a function of the particle sizes. The thermal hysteresis first remains as high as 12.5 K with the particle sizes decreasing to P278, and then starts to decrease largely to nearly 8 K for P4 with further reduction of the particle sizes. The decrease of thermal hysteresis implies the weakening of the first-order magnetic transition caused by the reduction of the particle sizes.

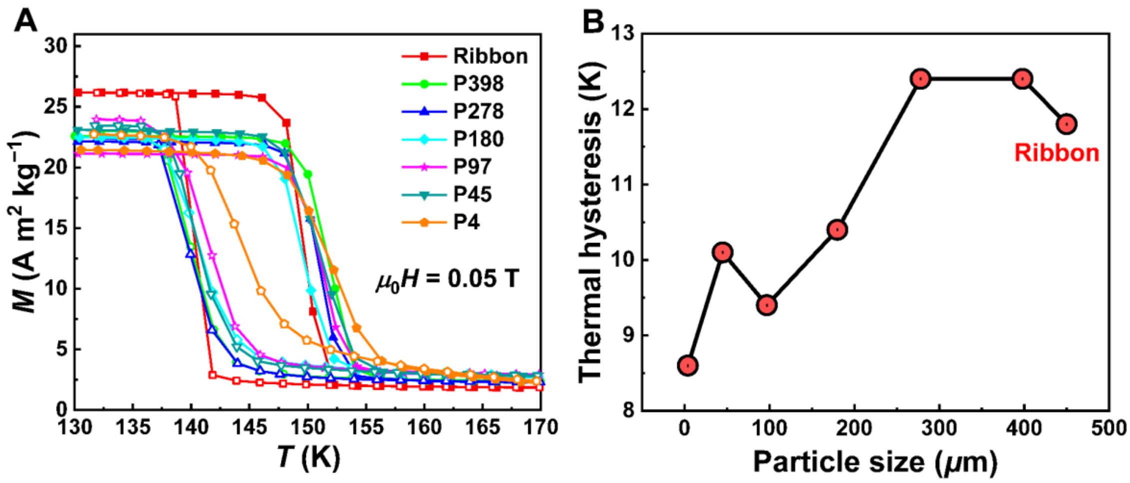

Supplementary Figure 4. (A) Temperature dependences of heating (solid symbol) and cooling (open symbol) magnetizations for $La_{0.7}Ce_{0.3}Fe_{11.51}Mn_{0.09}Si_{1.4}$ powders with different particle sizes under 0.05 T. (B) Thermal hysteresis as a function of particle size.

Supplementary Figure 5A shows the magnetization isotherms during the magnetization and demagnetization processes for the La-Fe-Si ribbon, P180, and P4, respectively. Obvious magnetic hysteresis is observed around the transition temperature, proving the nature of first-order magnetic transition. In addition, it could be noticed that the $La_{0.7}Ce_{0.3}Fe_{11.51}Mn_{0.09}Si_{1.4}$ compounds remain the field-induced itinerant electronic metamagnetic transition but the IEM transition becomes less sharp with the reduction of particle sizes. Supplementary Figure 5B shows the hysteresis loss (enclosed area in a field cycle) as a function of temperature for the corresponding samples. The maximum hysteresis loss decreases remarkably by 44% from 160 J/kg for the ribbons to 90 J/kg for the P4 sample. This confirms the weakening of first-order IEM transition with reduction of the particle sizes. Generally, the origins of hysteresis can be classified into the intrinsic factor (related to strain effect, impurity, frictions from domain rearrangements and electronic structure) and extrinsic factor (related to heat transfer and microstructure)[1]. For the La(Fe, Si)$_{13}$-based compounds, internal strain effect and frictions from domain rearrangements caused by strong magnetovolume effect will result in large hysteresis[2]. Previous studies indicate that introducing porous and altering sample geometry can result in partial removal of the internal strain and grain boundaries that restrain volume expansion, thus reducing the hysteresis[3,4]. Additionally, an improved heat transfer can also reduce extrinsic hysteresis[5]. Breaking the La-Fe-Si ribbons into particles can partially remove internal strain and grain boundaries. In addition, the specific surface areas of the samples could increase while the ribbons are ground into particles with smaller sizes, which can also remarkably improve their heat transfer. Therefore, the reduction of thermal and magnetic hysteresis in present study can be ascribed to the partially-removed internal strain and grain boundaries as well as the significantly increased specific surface areas of the samples.

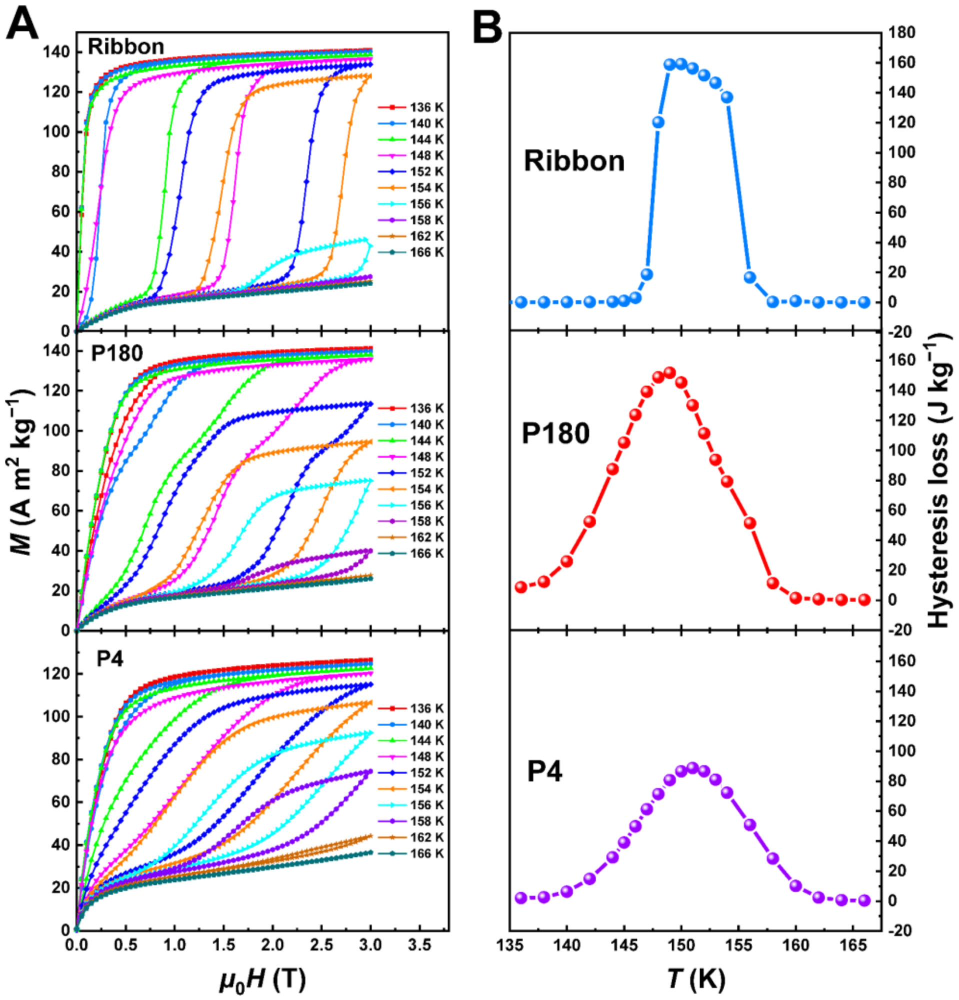

Supplementary Figure 5. (A) Magnetization isotherms with magnetizing and demagnetizing processes for ribbon, P180 and P4. (B) Hysteresis loss as a function of temperature for ribbon, P180 and P4.

In order to intuitively show the effect of the particle size on the first-order magnetic transition, the Arrott plot is applied to investigate the nature of magnetic transition for the $La_{0.7}Ce_{0.3}Fe_{11.51}Mn_{0.09}Si_{1.4}$ ribbons and powders. The magnetic transition is considered to be first-order when the Arrott plot exhibits negative slope or inflection point, while it is expected to be second-order when the slope is positive[6]. The Arrott plots of the $La_{0.7}Ce_{0.3}Fe_{11.51}Mn_{0.09}Si_{1.4}$ ribbons and different sized powders derived from magnetization isotherms near their T_Cs are displayed in Supplementary Figure 6. It can be seen that all curves show significant negative slopes, which confirms the nature of first-order magnetic transition. In addition, the negative slopes gradually decline with the reduction of the particle sizes, implying the weakening of first-order magnetic transition, which is consistent with the results of thermal and magnetic hysteresis. For La(Fe, Si)$_{13}$-based compounds, the hydrostatic pressure can strengthen the first-order nature of magnetic transition and enlarge the magnetovolume effect by compressing the intra-icosahedral Fe-Fe bonds in the structure[7]. During the transition of the bulk sample, the volume expansion of each individual grain is constrained by neighboring grains, resulting in the internal stress. When the ribbons are broken into particles, the partially removed internal strain and grain boundaries will reduce the internal constraints, that is, the internal stress is partially released. This will weaken the first-order magnetic transition and magnetovolume effect.

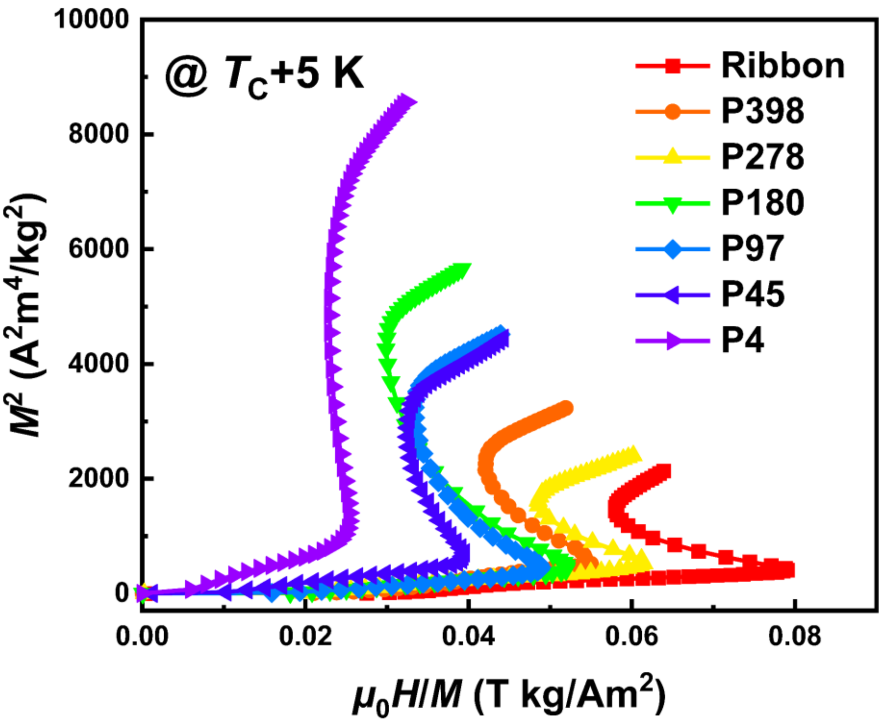

Supplementary Figure 6. Arrott plots of $La_{0.7}Ce_{0.3}Fe_{11.51}Mn_{0.09}Si_{1.4}$ powders with different particle sizes near their T_C.

The magnetic entropy change (ΔS_M) was calculated from the isothermal magnetization curves using the Maxwell relation[8]:

$$\Delta S_M(T,H) = \mu_0 \int_0^H \left(\frac{\partial M}{\partial T}\right)_H dH \quad \text{(S1)}$$

Supplementary Figure 7A shows the temperature dependence of $-\Delta S_M$ under a magnetic field change of 0–1 T for the $La_{0.7}Ce_{0.3}Fe_{11.51}Mn_{0.09}Si_{1.4}$ ribbons and powders with different particle sizes. The ΔS_M gradually decreases while the ΔS_M peak gradually widens with the reduced particle sizes, which means the weakening of the first-order magnetic transition. Supplementary Figure 7B plots the maximum $-\Delta S_M$ value as a function of the particle sizes. The maximum $-\Delta S_M$ value of the ribbon samples can reach as high as 21.5 J/kg K under a low magnetic field change of 0–1 T. This giant MCE implies that the $La_{0.7}Ce_{0.3}Fe_{11.51}Mn_{0.09}Si_{1.4}$ ribbon is a desirable magnetocaloric material. In addition, it is worth noting that the variation trend of $-\Delta S_M$ (Supplementary Figure 7B) is similar to the change of the thermal hysteresis (Supplementary Figure 4B) while reducing the particle sizes. The $-\Delta S_M$ shows small fluctuations while the average particle size is larger than 278 μm, and then the $-\Delta S_M$ gradually decreases while the average particle size is smaller than 278 μm. The significant change of internal strain and grain boundaries may not take place as the sample morphology changes from ribbon to powder with larger particle size (average particle size > 278 μm). In other words, the powders with large particle size will show similar performance to the ribbon. As the sample is further ground into finer powders (average particle size < 278 μm), the internal stress imposed by internal strain and grain boundaries will be gradually removed, thus weakening the first-order magnetic transition and decreasing the magnetic entropy change. Nevertheless, even though the weakening of the first-order magnetic transition caused by the reduction of particle size will decrease the magnetic entropy change, the $La_{0.7}Ce_{0.3}Fe_{11.51}Mn_{0.09}Si_{1.4}$ powder with an average particle size of ~4 μm can still obtain a maximum $-\Delta S_M$ value of 10.1 J/kg K under a low magnetic field change of 0–1 T, which is larger than those of many typical magnetocaloric materials[9,10].

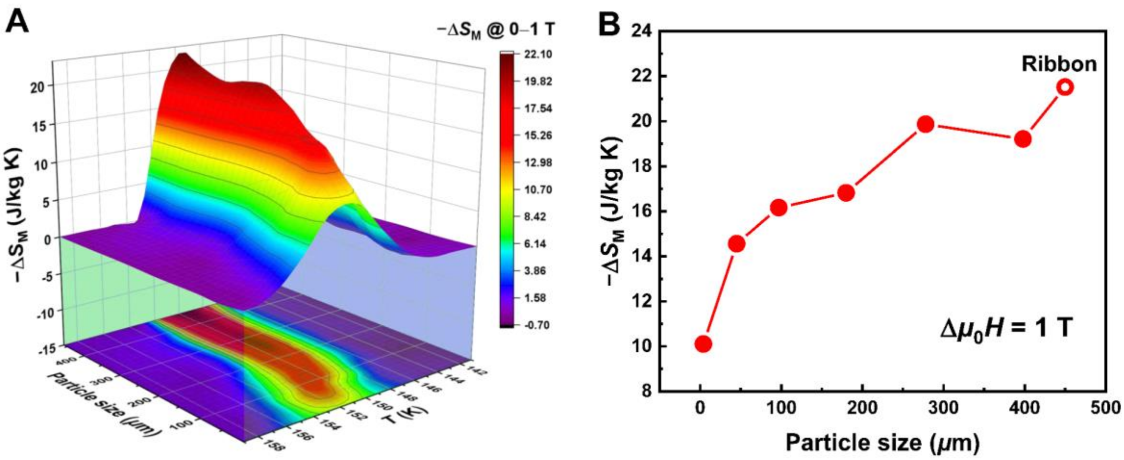

Supplementary Figure 7. (A) Temperature dependence of $-\Delta S_M$ under the magnetic field change of 0−1 T for La-Fe-Si powders with different particle sizes. (B) Maximum $-\Delta S_M$ value as a function of particle size.

Supplementary Figure 8A shows the XRD patterns of the P180 powders (120−240 μm) measured at different temperatures in a heating mode. $La_{0.7}Ce_{0.3}Fe_{11.51}Mn_{0.09}Si_{1.4}$ compound remains the cubic $NaZn_{13}$-type structure as well as the same phase composition through the magnetic transition. However, the diffraction peaks shift towards higher Bragg angle while the temperature increases from 60 K to 230 K. This result indicates the NTE behavior of the compound lattices according to the Bragg's law. Furthermore, the temperature dependence of the representative (531) diffraction peak is plotted in Supplementary Figure 8B. The (531) reflection peak shifts to higher 2θ angles with the increasing temperature, and exhibits an abrupt jump towards higher angle from 46.69° to 46.79° around 150 K. This relates to the NTE of the lattices during the magnetic transition. The lattice constant (a) of the $La_{0.7}Ce_{0.3}Fe_{11.51}Mn_{0.09}Si_{1.4}$ compound at different temperatures can be obtained by Rietveld refinement based on the temperature-variation XRD patterns. Supplementary Figure 8C shows the temperature dependence of the linear thermal expansion ($\Delta a/a$) for the $La_{0.7}Ce_{0.3}Fe_{11.51}Mn_{0.09}Si_{1.4}$ compound. The $\Delta a/a$ value decreases sharply with increasing temperature over 140 K to 160 K, i.e., the $La_{0.7}Ce_{0.3}Fe_{11.51}Mn_{0.09}Si_{1.4}$ compound undergoes a distinct negative thermal expansion. The average CTE of the $La_{0.7}Ce_{0.3}Fe_{11.51}Mn_{0.09}Si_{1.4}$ compound is determined to be -76.4×10^{-6} K^{-1} in the NTE region from 100 K to 180 K. This large NTE coefficient implies the excellent NTE properties of $La_{0.7}Ce_{0.3}Fe_{11.51}Mn_{0.09}Si_{1.4}$ compound.

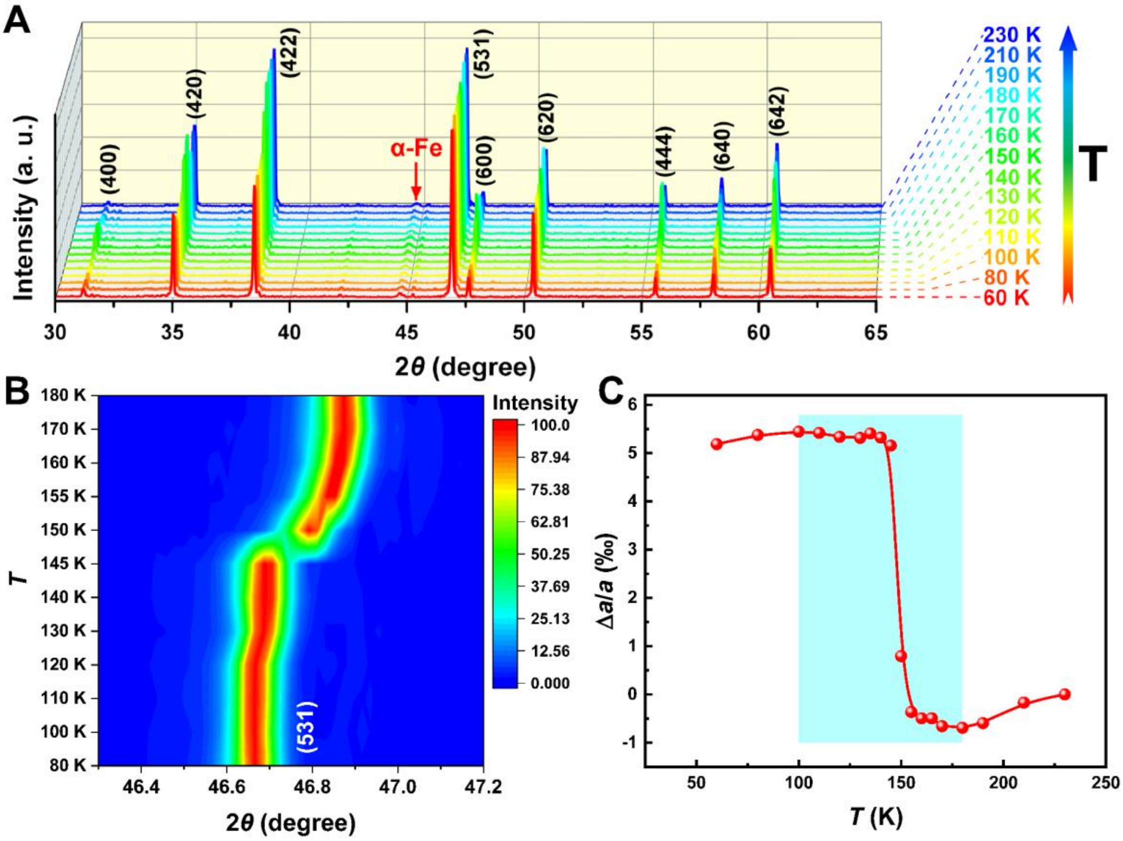

Supplementary Figure 8. (A) XRD patterns of La-Fe-Si compound measured at different temperatures. (B) Temperature dependence of (531) diffraction peak for La-Fe-Si compound. (C) Temperature dependent linear thermal expansion ($\Delta a/a$) for La-Fe-Si compound.

Supplementary Figure 9 shows the BSE image of a produced La-Fe-Si/resin composite with 3 wt.% resin and the corresponding elemental mapping of La, Ce, Fe, Mn, Si and C elements. La, Ce, Fe, Mn and Si elements are found to be homogeneously distributed in the $La_{0.7}Ce_{0.3}Fe_{11.51}Mn_{0.09}Si_{1.4}$ particles, and the C is from the epoxy resin.

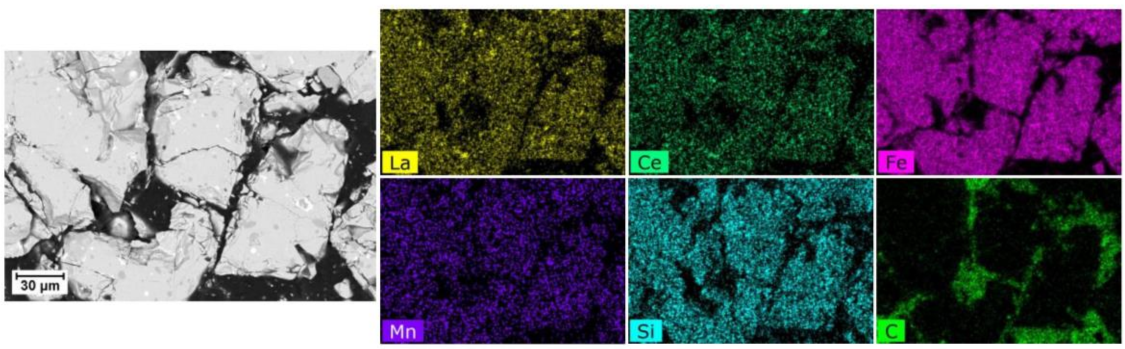

Supplementary Figure 9. Backscattered electron image of La-Fe-Si/resin composite with 3 wt.% resin and related elemental mapping of La, Ce, Fe, Mn, Si and C elements.

Supplementary Figure 10 shows the backscattered electron (BSE) and secondary electron (SE) images of the P180 composite. The resins and pores both present as black areas in the BSE image, but from the SE image, it is found that the pores are darker and bigger areas compared with the resin regions.

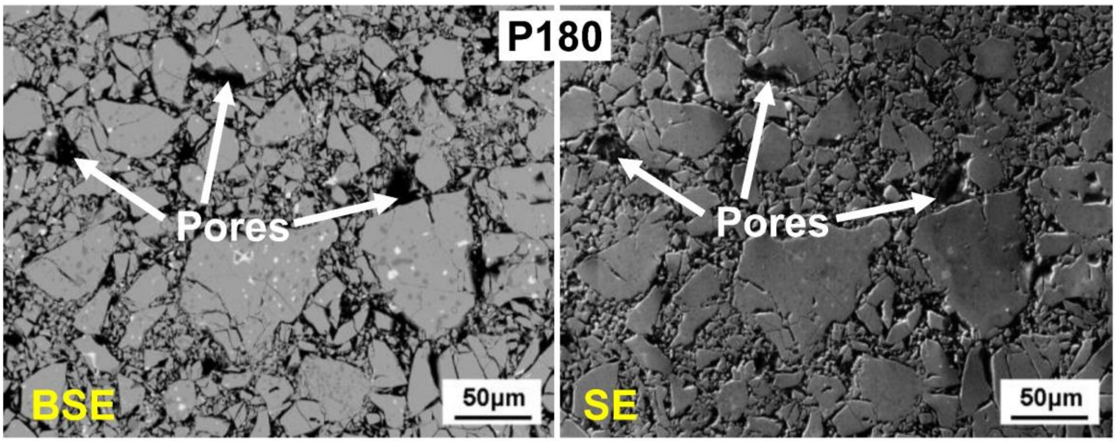

Supplementary Figure 10. Backscattered electron and secondary electron images of P180 composite.

Supplementary Figure 11 shows the XRD patterns of La-Fe-Si powder, Resin3, Resin20 and Resin80 composites. It can be found that the composites are composed of the characteristic peaks of La-Fe-Si powders and the broad peak from epoxy resin. Moreover, no impurity phase is observed for the composites, indicating that the pressing process does not cause the instability of the La-Fe-Si phase.

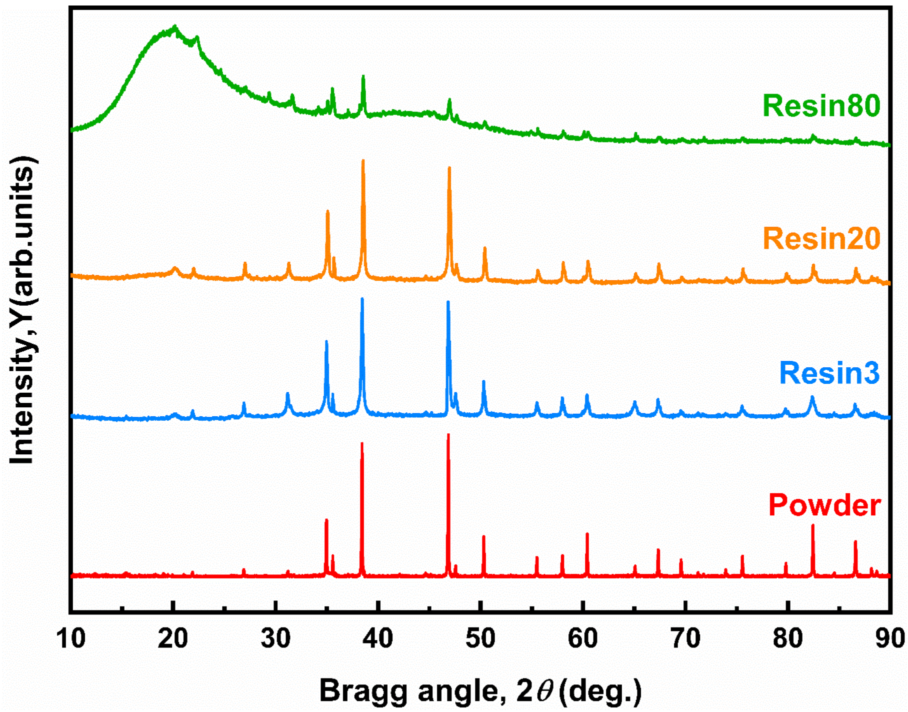

Supplementary Figure 11. XRD patterns of La-Fe-Si powders, Resin3, Resin20 and Resin80 composites.

Supplementary Figure 12 shows the DSC heat flow curves of La-Fe-Si powders, Resin3, Resin20 and Resin80 composites. The La-Fe-Si powders and the composites with different resin contents exhibit consistent DSC peaks, which implies that the epoxy resin will not affect the first-order magnetic transition of La-Fe-Si compound. However, it can be observed that the Resin20 and Resin80 composites show wider DSC peaks, which may be attributed to the poor thermal conductivity of the Resin20 and Resin80 composites.

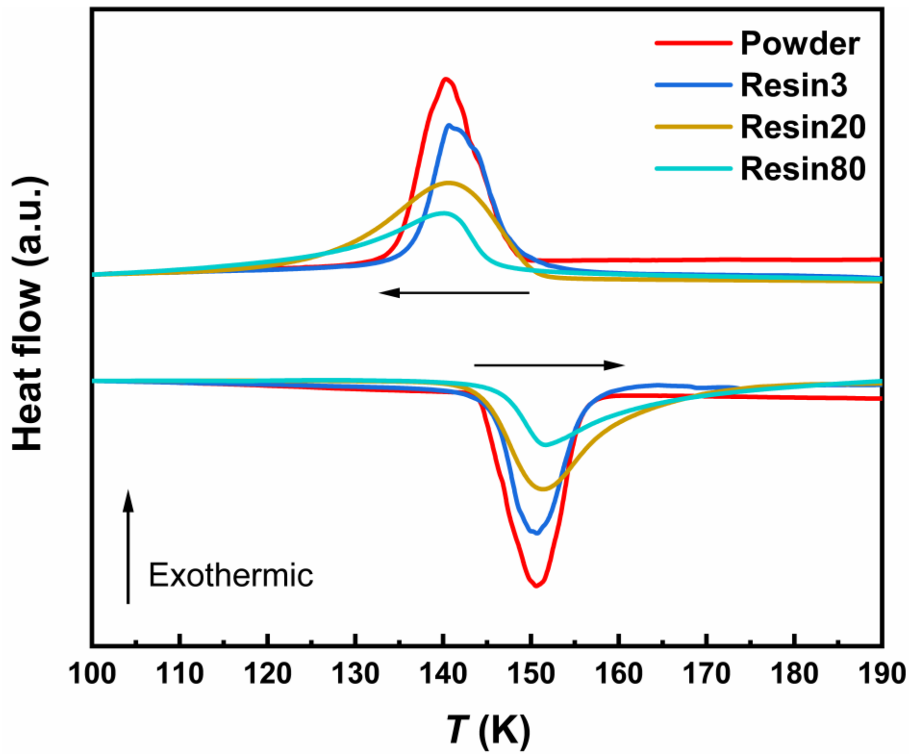

Supplementary Figure 12. DSC heat flow curves of La-Fe-Si powders, Resin3, Resin20 and Resin80 composites.

Supplementary Figure 13A shows the theoretical thermal expansion of the La-Fe-Si/resin composites with different resin contents. Then, the coefficient of thermal expansion of La-Fe-Si/resin composites with different resin contents can be calculated. Supplementary Figure 13B shows the experimental and theoretical values of coefficients of thermal expansion of the composites in the magnetic transition temperature range. It can be seen that both theoretical and experimental values gradually decrease with the increase of resin content. Moreover, the experimental values are lower than the theoretical values. The thermal expansion obtained from the temperature-variation XRD measurement may deviate from the actual thermal expansion of the La-Fe-Si compound. In addition, the existence of pores in the composites will affect the thermal expansion of the composites. Therefore, the experimental values of coefficients of thermal expansion are different from the theoretical values.

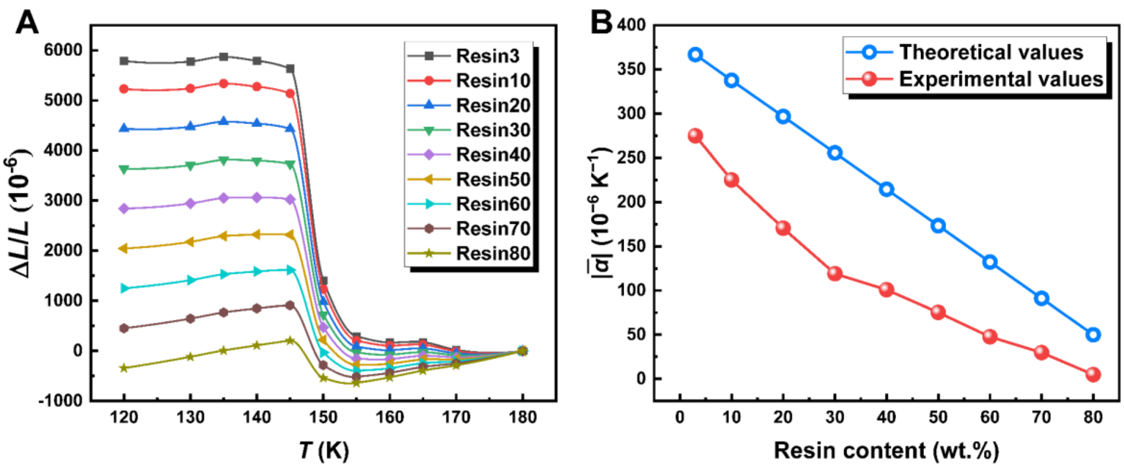

Supplementary Figure 13. (A) Temperature dependence of theoretical thermal expansion for La-Fe-Si/resin composites with different resin contents. (B) Experimental and theoretical values of coefficients of thermal expansion of the composites in the magnetic transition temperature range.

REFERENCES

1. Gutfleisch O, Gottschall T, Fries M, et al. Mastering hysteresis in magnetocaloric materials. *Phil Trans R Soc A* 2016;374:20150308. [DOI: 10.1098/rsta.2015.0308]
2. Hu FX, Chen L, Wang J, et al. Particle size dependent hysteresis loss in $La_{0.7}Ce_{0.3}Fe_{11.6}Si_{1.4}C_{0.2}$ first - order systems. *Appl Phys Lett* 2012;100:072403. [DOI: 10.1063/1.3684244]
3. Lyubina J, Schafer R, Martin N, Schultz L, Gutfleisch O. Novel design of $La(Fe,Si)_{13}$ alloys towards high magnetic refrigeration performance. *Adv Mater* 2010;22:3735-9. [DOI: 10.1002/adma.201000177]
4. Huang JH, Sun NK, Liu CL, et al. Effect of particle size on the hysteretic behavior and magnetocaloric effect of $La_{0.5}Pr_{0.5}Fe_{11.4}Si_{1.6}$ compound. *Acta Metall Sin (Engl Lett)* 2014;27:27-30. [DOI: 10.1007/s40195-014-0031-9]
5. Moore JD, Morrison K, Sandeman KG, Katter M, Cohen LF. Reducing extrinsic

hysteresis in first-order La(Fe,Co,Si)$_{13}$ magnetocaloric systems. *Appl Phys Lett* 2009;95:252504. [DOI: 10.1063/1.3276565]

6. Banerjee SK. On a generalised approach to first and second order magnetic transitions. *Phys Lett* 1964;12:16-7. [DOI: 10.1016/0031-9163(64)91158-8]

7. Hao JZ, Hu FX, Wang JT, et al. Large enhancement of magnetocaloric and barocaloric effects by hydrostatic pressure in $La(Fe_{0.92}Co_{0.08})_{11.9}Si_{1.1}$ with a $NaZn_{13}$-type structure. *Chem Mater* 2020;32:1807-18. [DOI: 10.1021/acs.chemmater.9b03915]

8. Franco V, Blázquez JS, Ingale B, Conde A. The magnetocaloric effect and magnetic refrigeration near room temperature: materials and models. *Annu Rev Mater Res* 2012;42:305-42. [DOI: 10.1146/annurev-matsci-062910-100356]

9. Wei ZY, Liu EK, Li Y, et al. Unprecedentedly wide Curie-temperature windows as phase-transition design platform for tunable magneto-multifunctional materials. *Adv Electron Mater* 2015;1:1500076. [DOI: 10.1002/aelm.201500076]

10. Phan TL, Zhang P, Dan NH, et al. Coexistence of conventional and inverse magnetocaloric effects and critical behaviors in $Ni_{50}Mn_{50-x}Sn_x$ (x = 13 and 14) alloy ribbons. *Appl Phys Lett* 2012;101:212403. [DOI: 10.1063/1.4767453]